AGU PUBLICATIONS

JGR

Journal of Geophysical Research: Solid Earth

RESEARCH ARTICLE
10.1002/2015JB011963

**Key Points:**
- Comprehensive laboratory study of faults at SAFOD
- Creeping faults are frictionally weak, slide stably, and exhibit no healing
- Results consistent with observed creep and microearthquakes

**Supporting Information:**
- Table S1
- Table S2
- Tables S1 and S2

**Correspondence to:**
B. M. Carpenter,
brett.carpenter@ingv.it

**Citation:**
Carpenter, B. M., D. M. Saffer, and C. Marone (2015), Frictional properties of the active San Andreas Fault at SAFOD: Implications for fault strength and slip behavior, *J. Geophys. Res. Solid Earth*, *120*, 5273–5289, doi:10.1002/2015JB011963.

Received 16 FEB 2015
Accepted 17 JUN 2015
Accepted article online 18 JUN 2015
Published online 14 JUL 2015



# Frictional properties of the active San Andreas Fault at SAFOD: Implications for fault strength and slip behavior

**B. M. Carpenter[1,2], D. M. Saffer[2], and C. Marone[2]**

[1]Istituto Nazionale di Geofisica e Vulcanologia, Rome, Italy, [2]Department of Geosciences and Energy Institute Center for Geomechanics, Geofluids, and Geohazards, Pennsylvania State University, University Park, Pennsylvania, USA

**Abstract** We present results from a comprehensive laboratory study of the frictional strength and constitutive properties for all three active strands of the San Andreas Fault penetrated in the San Andreas Observatory at Depth (SAFOD). The SAFOD borehole penetrated the Southwest Deforming Zone (SDZ), the Central Deforming Zone (CDZ), both of which are actively creeping, and the Northeast Boundary Fault (NBF). Our results include measurements of the frictional properties of cuttings and core samples recovered at depths of ~2.7 km. We find that materials from the two actively creeping faults exhibit low frictional strengths ($\mu$ = ~0.1), velocity-strengthening friction behavior, and near-zero or negative rates of frictional healing. Our experimental data set shows that the center of the CDZ is the weakest section of the San Andreas Fault, with $\mu$ = ~0.10. Fault weakness is highly localized and likely caused by abundant magnesium-rich clays. In contrast, serpentine from within the SDZ, and wall rock of both the SDZ and CDZ, exhibits velocity-weakening friction behavior and positive healing rates, consistent with nearby repeating microearthquakes. Finally, we document higher friction coefficients ($\mu > 0.4$) and complex rate-dependent behavior for samples recovered across the NBF. In total, our data provide an integrated view of fault behavior for the three active fault strands encountered at SAFOD and offer a consistent explanation for observations of creep and microearthquakes along weak fault zones within a strong crust.

## 1. Introduction

Understanding the frictional, hydrologic, and mechanical behaviors of tectonic plate boundary fault systems, including the San Andreas Fault (SAF), has been the focus of many recent fault zone drilling projects [e.g., *Kinoshita et al*., 2009; *Townend et al*., 2009; *Zoback et al*., 2011]. These initiatives have recovered samples of fault rock and gouge and conducted measurements of in situ stress, fluid chemistry, and temperature at depths where earthquakes nucleate. Samples and data emerging from these drilling projects provide an unparalleled opportunity to gain new insight into absolute fault strength [e.g., *Brune et al*., 1969; *Zoback et al*., 1987; *Scholz*, 2000; *Carpenter et al*., 2012], causes of apparent fault weakness [e.g., *Rice*, 1992; *Faulkner and Rutter*, 2001; *Brantut et al*., 2011; *Gratier et al*., 2011; *Lockner et al*., 2011], and the laws that govern fault slip and failure [e.g., *Dieterich*, 1979; *Marone*, 1998a; *Ikari et al*., 2009; *Carpenter et al*., 2011; *Sone et al*., 2012].

The San Andreas Fault Observatory at Depth (SAFOD) drilling project was a multiphase project that penetrated three active strands of the San Andreas Fault (SAF) near Parkfield, California, at a depth of ~2.7 km (Figure 1). The borehole is located near the southern terminus of the central creeping section of the SAF [*Titus et al*., 2006], to the NW of the epicenter of the $M_w$ 6.0, 2004 Parkfield earthquake. Drilling penetrated to 3.2 km true vertical depth (TVD) [*Zoback et al*., 2011], through Salinian granite and arkosic sandstone of the Pacific Plate, across the SAF, and ended in the Great Valley Formation of the North American Plate (Figure 1).

The SAFOD project was implemented in four phases, including a pilot hole and three phases of main hole drilling [*Hickman et al*., 2004; *Zoback et al*., 2011]. The Pilot Hole drilled in 2002 is near vertical to a TVD of 2.2 km within the Pacific Plate. It returned cuttings and produced a suite of geophysical logs and in situ measurements of stress and heat flow. Phase I of the Main Hole deviated toward the fault and reached a TVD of ~2.5 km in 2004, stopping just short of the SAF in order to case the borehole, and returned cuttings, approximately 20 m of core, and geophysical logs. Phase II drilling in 2005 crossed the SAF and penetrated into the Great Valley Formation of the North American Plate, extending to a TVD of ~3 km.

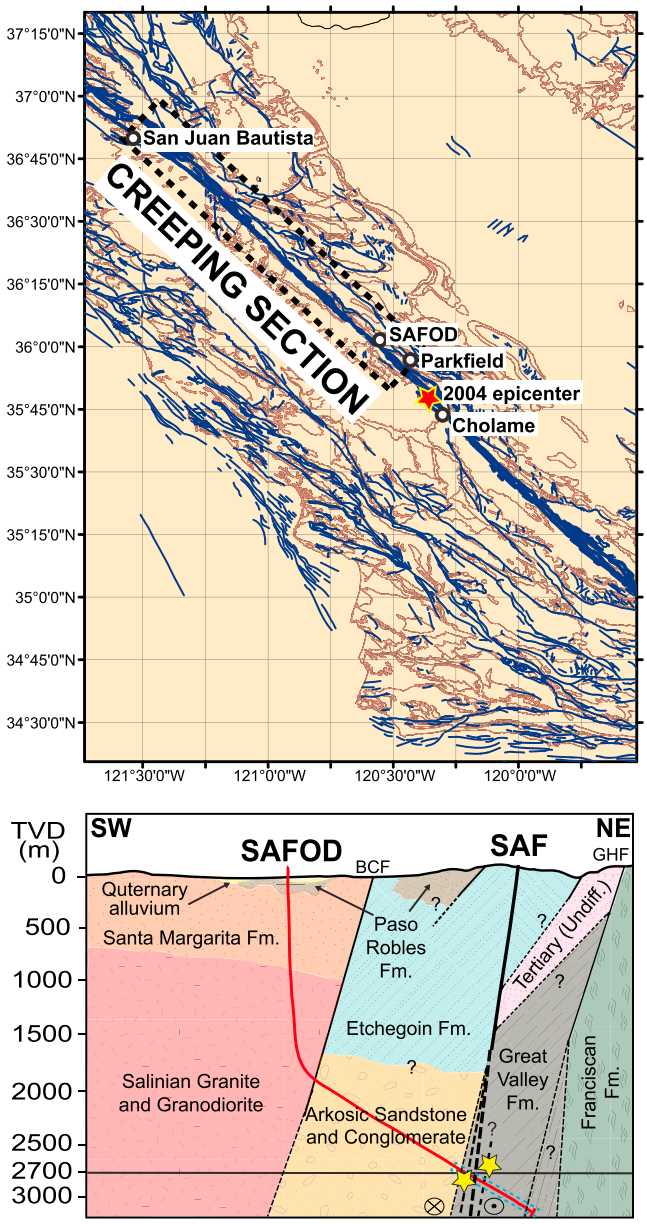


**Figure 1.** (top) Locations of the SAFOD borehole, epicenter of the 2004 Parkfield earthquake, and approximate boundary of the creeping segment on topographic (pink lines) base map with faults (dark blue lines) as compiled by *Dibblee* [1973]. (bottom) Geologic cross section [*Thayer et al.*, 2004; *Zoback et al.*, 2011] at the location of the SAFOD borehole (red line). The stars indicate the approximate positions of repeating earthquake clusters. The blue dashed box indicates the approximate location of the geophysical logs shown in Figure 2.

Phase II returned drill cuttings, 3.7 m of spot core, 52 sidewall cores, and geophysical logs. Repeat caliper logs inside the casing identified two actively creeping fault strands—the Southwest Deforming Zone (SDZ) and Central Deforming Zone (CDZ). Phase III drilling was completed in 2007 and returned cuttings and ~40 m of core that spanned the two actively creeping faults. Additional details of the SAFOD project are described by *Zoback et al.* [2011].

Phases I–III of SAFOD drilling in the Main Hole returned a range of samples from the fault zone and adjacent wall rock, including drill cuttings across the three actively slipping strands of the SAF and intact core across two of these strands [*San Andreas Observatory at Depth* (*SAFOD*), 2010]. The zones of active slip were first defined in geophysical logs collected after Phase II, in combination with lithologic changes noted in drill cuttings [*Solum et al.*, 2006] (Figure 2). In total, four primary structures were identified across the ~200 m wide San Andreas Fault and damage zone (Figure 2):

1. A primary geologic boundary at 3150 m measured depth (MD) that marks the contact between arkosic sandstone of the Pacific Plate and shale/siltstone of the Great Valley Sequence of the North American Plate. This boundary is interpreted to be the ancestral (now inactive) SAF.
2. The Southwest Deforming Zone (SDZ) at 3192 m MD, a fault characterized by active creep over a 1.5 m wide gouge zone documented by casing deformation [*Zoback et al.*, 2011]. This marks the southwest edge of the interpreted 200 m wide modern SAF zone and lies ~100 m vertically above the *M*~2.0 "Hawaii" cluster of repeating earthquakes [*Thurber et al.*, 2010].
3. The Central Deforming Zone (CDZ) at 3302 m MD, characterized by a 2.6 m wide gouge zone and significant casing deformation. This is the primary strand of active creep at the depth of the SAFOD hole.
4. The Northeast Boundary Fault (NBF) at 3413 m MD, characterized by changes in sonic velocity and lithology (Figure 2). This marks the northeast edge of the interpreted SAF zone and is thought to host the *M*~2.0 "Los Angeles" and "San Francisco" repeating earthquake clusters located updip of the SAFOD borehole intersection with the fault [*Thurber et al.*, 2010].

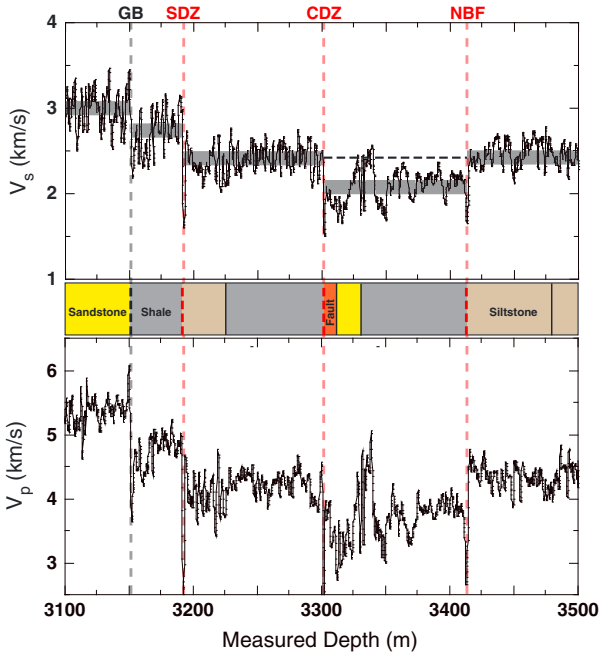


**Figure 2.** Sonic velocity logs from SAFOD Phase II borehole showing the geologic boundary (black dashed line), lithologic units [*Solum et al.*, 2006], and faults (red dashed lines): SDZ = Southwest Deforming Zone, CDZ = Central Deforming Zone, and NBF = Northeast Boundary Fault.

A number of recent studies have reported on the frictional properties of materials returned from the SAFOD project, as well as outcrop samples of rock units that abut the fault at depth [e.g., *Tembe et al.*, 2006; *Carpenter et al.*, 2009, 2011, 2012; *Gratier et al.*, 2011; *Lockner et al.*, 2011; *Coble et al.*, 2014; *French et al.*, 2015]. These studies show that the crust surrounding the fault is frictionally strong but that the active San Andreas Fault is weak. Drill cuttings from the country rock exhibit friction values consistent with Byerlee's law ($\mu = 0.40$–$0.66$) [*Tembe et al.*, 2006; *Carpenter et al.*, 2009], whereas clay and serpentine grains separated from the cuttings are slightly weaker ($\mu = 0.30$–$0.50$) [*Morrow et al.*, 2007]. Experiments on cuttings from the CDZ document a low coefficient of friction ($\mu < 0.25$), low (near-zero) rates of frictional healing, and strong localization of these mechanical properties to the creeping gouge zone [*Carpenter et al.*, 2011]. These behaviors are correlated with the presence of magnesium-rich clays, suggesting that clay mineralogy is an important control on the strength and healing behavior of the fault, at least at these depths [e.g., *Schleicher et al.*, 2010; *Bradbury et al.*, 2011; *Holdsworth et al.*, 2011; *Hadizadeh et al.*, 2012; *Richard et al.*, 2014].

Experiments performed on powdered core from within and surrounding both the SDZ and CDZ show that abundant magnesium-rich clay (saponite and corrensite) localized within the faults results in low frictional strength ($\mu < 0.15$), whereas the surrounding rock is stronger ($\mu = 0.3$–$0.6$) [*Carpenter et al.*, 2011; *Lockner et al.*, 2011; *Coble et al.*, 2014]. This is consistent with several studies that have documented the important role of gouge composition—and clay content in particular—on frictional properties [e.g., *Lupini et al.*, 1981; *Logan and Rauenzahn*, 1987; *Brown et al.*, 2003; *Ikari et al.*, 2009]. In other cases, fault weakness arises from a combination of shear fabric and phyllosilicate content [e.g., *Collettini et al.*, 2009, 2011; *Ikari et al.*, 2011; *Haines et al.*, 2013; *Warr et al.*, 2014].

Experiments performed on intact core samples recovered across the CDZ [*Carpenter et al.*, 2012] show that the actively creeping fault is weak ($\mu < 0.1$) and document an abrupt transition to stronger wall rock ($\mu > 0.4$) over a distance of less than 0.5 m. *Carpenter et al.* [2012] reported velocity-strengthening frictional behavior for material from the CDZ, and instances of velocity-weakening behavior in wall rock to the NE, raising the possibility that earthquakes could nucleate in wall rock. Furthermore, because clay-rich gouge is observed to transition to pressure-independent shear strength at effective normal stresses above ~40–60 MPa [e.g., *Saffer and Marone*, 2003], *Carpenter et al.* [2012] suggested that the strength of the CDZ might remain nearly constant in the upper ~8 km rather than increasing linearly as is commonly assumed for faults in the brittle crust. The values of $\mu$ (and estimates of in situ shear strength) derived from experiments on core samples of the CDZ are sufficiently low to explain the apparent weakness of the SAF as inferred from both heat flow and directional constraints [*Lachenbruch and Sass*, 1980; *Zoback et al.*, 1987; *Hickman and Zoback*, 2004; *Lockner et al.*, 2011; *Carpenter et al.*, 2012; *Coble et al.*, 2014].

A number of laboratory studies have been conducted on SAFOD samples. However, many of these included a limited suite of drill cuttings or powdered samples and did not include measurements on intact fault rock. To date, a comprehensive view of the frictional strength and constitutive properties spanning the active SAF

**Table 1.** SAFOD Experimental Samples [*Carpenter et al.*, 2012]*

| Sample | Depth (m MD) | Wall/Fault | $\mu_{ss}$ at 25 MPa | $\beta$ at 25 MPa | Related Fault |
|---|---|---|---|---|---|
| G25 | 3189.9 | W | 0.60 | 0.0077 | SDZ (core) |
| G26 | 3190.6 | W | 0.36 | 0.0066 | |
| G27-1 | 3191.5 | F | 0.15 | −0.0012 | |
| G27-2 | 3191.7 | F-SERP. | 0.51 | 0.0039 | |
| G27-3 | 3191.9 | F-SERP. | 0.40 | 0.0036 | |
| G27-4 | 3191.9 | F-SERP. | 0.42 | 0.0018 | |
| G27-5 | 3192.1 | F | 0.13 | −0.0010 | |
| G28 | 3192.4 | F | 0.13 | −0.0011 | |
| G29 | 3192.9 | F-SERP. | 0.29 | 0.0018 | |
| G31 | 3193.8 | W | 0.43 | 0.0031 | |
| G32 | 3194.1 | W | 0.45 | 0.0036 | |
| G41 | 3298.4 | W | 0.49 | 0.0049 | CDZ (core) |
| G42A* | 3299.7 | W | 0.49 | 0.0049 | |
| G42B* | 3300.5 | F | 0.25 | 0.0013 | |
| G43A* | 3300.9 | F | 0.10–0.18 | 0.00018–0.0017 | |
| G43B* | 3301.3 | F | 0.14 | −0.0010 | |
| G44* | 3302.0 | F | 0.10 | −0.0012 | |
| G45A* | 3302.7 | F | 0.29 | −0.0023 | |
| G45B | 3303.0 | W | 0.41 | −0.0006 | |
| G46* | 3303.6 | W | 0.50–0.48 | 0.0024–0.0075 | |
| G51 | 3304.1 | W | 0.47 | 0.0032 | |
| 11150 | 3398.5 | W | 0.43 | 0.0035 | NBF (cuttings) |
| 11180 | 3407.7 | W | 0.42 | 0.0058 | |
| 11190 | 3410.7 | W | 0.46–0.44 | 0.0057–0.0053 | |
| 11200 | 3413.8 | W | 0.44–0.46 | 0.0038–0.0043 | |
| 11210 | 3416.8 | W | 0.42 | 0.0052 | |
| 11220 | 3419.9 | W | 0.43 | 0.0042 | |
| 11250 | 3429.0 | W | 0.46 | 0.0070 | |

*Asterisk indicates data/samples previously published in *Carpenter et al.* [2012].

system is lacking. Here we expand on previous studies by (1) reporting data for strength and friction constitutive properties spanning all three active fault strands penetrated by SAFOD drilling, including the NBF; (2) presenting detailed data describing the dependence of friction constitutive properties on normal stress and velocity for material from the CDZ; and (3) exploring the implications of our data set, that transects the whole of the active fault zone at SAFOD, for fault strength and observed modes of fault slip.

## 2. Methods

### 2.1. Experimental Materials

We tested a suite of drill cuttings and core samples spanning each of the three active SAFOD fault strands (Table 1). For the NBF, our samples include seven sets of drill cuttings, collected every ~3 m during Phase II (no cores were taken across the NBF). For the SDZ and CDZ, we studied both intact fault rock and powdered samples obtained from coring during Phase III drilling. For the SDZ, we performed experiments on 11 samples, including two samples of wall rock to the SW, three samples of fault gouge, four samples of serpentine from within the fault zone, and two samples of wall rock to the NE. For the CDZ, we conducted experiments on 10 samples, including two from wall rock to the SW, five samples of fault gouge, and three samples of wall rock to the NE [*Carpenter et al.*, 2012]. All reported measured depths for our samples have been registered to Phase II downhole geophysical logs (Figure 2) [*SAFOD*, 2010].

Wall rock on the SW side of the SDZ is described as a hard, massive gray-black shale [*SAFOD*, 2010]. Compositionally, it is dominated by smectite, quartz, and feldspar, with minor amounts of illite and chlorite/kaolinite (Table S1 in the supporting information). The foliated fault gouge of the SDZ is composed of an intensely sheared, noncohesive matrix surrounding polished porphyroclasts of the surrounding wall rock and serpentine. It is characterized by high clay content (>80 wt %; Table S1) [*Lockner et al.*, 2011] and in some areas contains abundant chrysotile. Corrensite has been identified as the main clay species present [*Lockner et al.*, 2011]. Several intact blocks of serpentine were also recovered

from the SDZ; these are highly fractured and contain calcite veins. These blocks are composed dominantly of lizardite, with increased chrysotile content in blocks that are more intensely sheared (D. Moore, personal communications). Wall rock on the NE side of the fault is composed of sheared thinly bedded shales and siltstones and contains more clay and less feldspar than wall rock to the SW (Table S1).

Wall rock on the SW side of the CDZ is primarily sheared siltstone and sandstone. X-ray diffraction (XRD) analysis shows that it is composed mainly of quartz and feldspar, with minor amounts of smectite, illite, chlorite/kaolinite, and calcite (Table S1). Foliated gouge from within the CDZ is macroscopically similar to the gouge observed in the SDZ, with zones of intensely sheared, noncohesive gouge surrounding elongated and polished porphyroclasts of wall rock and serpentine. XRD analysis of CDZ gouge indicates that saponite is the main smectite species present [*Lockner et al*., 2011; *Carpenter et al*., 2012] and that the total smectite content varies across the fault but is consistently higher than 80 wt %. Within the CDZ, quartz and feldspar are present only in minor amounts. Wall rock to the NE of the CDZ is composed of highly sheared siltstones and mudstones, containing abundant quartz, feldspar, and calcite, with overall clay content decreasing with distance from the fault (Table S1). Examination of core containing the CDZ indicates the presence of both Mg-rich clay (saponite) coatings [*Schleicher et al*., 2010] and thick, Mg-rich clay zones throughout the active fault [*Holdsworth et al*., 2011].

To date, samples surrounding the NBF have been less extensively characterized than the SDZ and CDZ, primarily because this fault strand was sampled only by drill cuttings. *Solum et al*. [2006] interpreted a lithologic break across the fault (Figure 2); rocks to the southwest of the NBF are shale dominated, whereas those to the northeast are primarily siltstones. XRD analysis of our cuttings documents a composition of ~50% quartz + feldspar, ~10% smectite, ~10% illite, and ~25% chlorite + kaolinite, with a slight increase in quartz and decrease in chlorite/kaolinite across the fault (Table S1).

### 2.2. Experimental Methods

#### 2.2.1. Experimental Procedure

We performed shearing experiments on both intact fault rock obtained from core and on powdered cuttings. Cuttings were washed with local surface water at the SAFOD drill site and then air dried before packaging. Once obtained from storage, a magnet was run through the cuttings to remove small slivers of casing, and they were dried at 40°C before being pulverized and sieved to $<125\,\mu m$ [*Carpenter et al*., 2011]. Rubble derived from the core was prepared in the same way as the cuttings. Wafers of intact fault rock were cut by shaping material from the core in an orientation parallel to shear, as identified by the core axis and visual observation of the macroscopic shear fabric [*Carpenter et al*., 2012]. Intact samples of gouge were kept at 100% relative humidity until used in experiments. For powdered gouge, we sheared specimens in a double-direct shear configuration (Figure 3) (see *Ikari et al*. [2009] for details). For intact fault rock, due to the limited volume of material available, we sheared samples in a single-direct shear configuration (Figure 3) [e.g., *Carpenter et al*., 2012].

All experiments were conducted under controlled conditions of constant effective normal stress ($\sigma_n'$), confining pressure ($P_c$), and pore pressure ($P_p$). Samples were saturated with a synthetic brine designed to match the major ion chemistry ($Na^+$, $Ca^{2+}$, $K^+$, and $Cl^-$) measured in the SAFOD borehole [*Thordsen et al*., 2005]. Most of our experiments were performed at 25 MPa effective normal stress in order to compare the behavior and constitutive properties of all three faults under similar conditions. For powdered fault gouge and intact wafers of the CDZ, we also explored a range of effective normal stresses from 7 to 100 MPa [*Carpenter et al*., 2012].

Samples were first assembled as shown in Figure 3, jacketed, and saturated under a confining pressure ($P_c$) of 1.0 MPa and an effective normal stress ($\sigma_n'$) of 1.5 MPa. Effective stress was then increased to the target value, and the sample was allowed to equilibrate until specimen pore pressure and layer thickness stabilized. After equilibration, a shear "run-in" at 10 μm/s was performed in each experiment to develop a steady state shear fabric and to define the coefficient of friction ($\mu$) (Figure 4). We report friction coefficient as the ratio of shear stress to effective normal stress, assuming zero cohesion. Following the run-in, we conducted a series of velocity-stepping and slide-hold-slide tests to measure friction constitutive properties (Figures 4 and 5) [e.g., *Dieterich*, 1979; *Ruina*, 1983]. We stepped sliding velocity in a sequence from 1 to 300 μm/s for the majority of our experiments and conducted holds ranging from 3 to 1000 s.

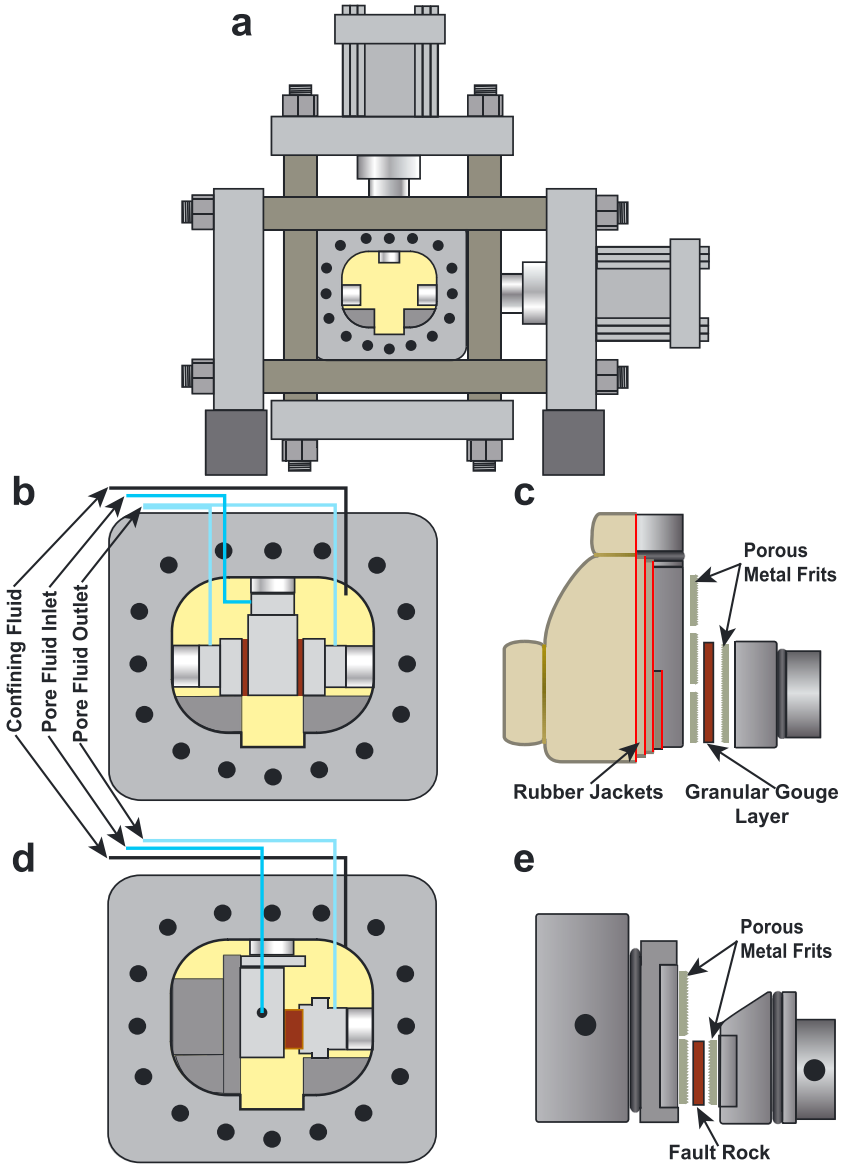


**Figure 3.** (a) Biaxial testing apparatus and pressure vessel for true triaxial loading. (b) Double-direct sample assembly with fluid plumbing shown. The double-direct shear (DDS) assembly is used for experiments conducted on all powdered (gouge) samples. (c) Details of DDS sample jacketing and fluid distribution frits. (d) Single-direct shear (SDS) sample assembly with fluid plumbing shown. The single-direct shear assembly is used for experiments conducted on intact samples of fault rock. (e) Detailed view of the SDS sample assembly and fluid distribution frits.

### 2.2.2. Friction Constitutive Properties

From our velocity-stepping experiments, we describe the rate dependence of friction using the friction rate parameter $(a-b)$:

$$(a-b) = \Delta\mu_{ss}/\Delta \ln V, \quad (1)$$

where $\mu_{ss}$ is the steady state friction coefficient and $V$ is the sliding velocity. Positive values of $(a-b)$, termed velocity strengthening, are associated with stable sliding and inhibit rupture nucleation [*Gu et al.*, 1984]. Negative values, termed velocity weakening, are a prerequisite for unstable slip and earthquake nucleation. We determined values of $a-b$ and other constitutive parameters (Figure 5) by fitting our data using an inverse modeling technique [e.g., *Reinen and Weeks*, 1993; *Blanpied et al.*, 1998] with the Dieterich (aging) law for friction with two state variables [*Marone*, 1998a]:

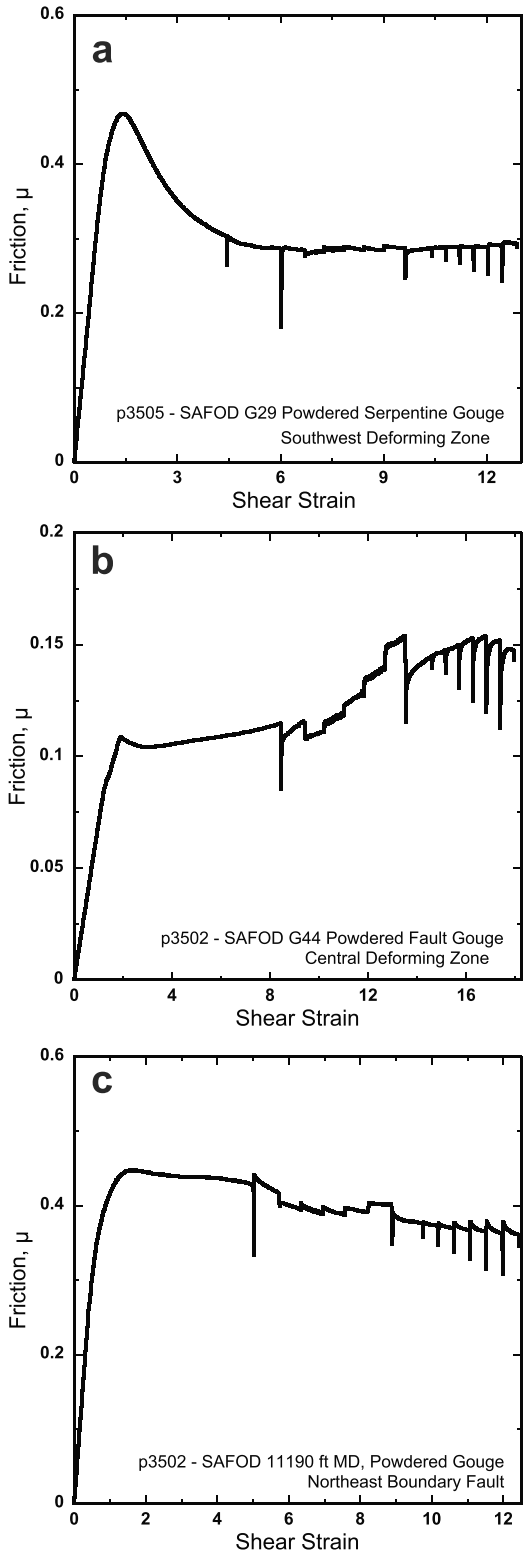


**Figure 4.** Raw data from shearing experiments on (a) powdered serpentine gouge from the SDZ, (b) powdered fault gouge from the CDZ, and (c) powdered cuttings from the NBF. All experiments were conducted at 25 MPa effective normal stress. After run-in at 10 μm/s, velocity steps and slide-hold-slide tests were performed to evaluate frictional velocity dependence and frictional healing.

$$\mu = \mu_0 + a \ln (V/V_0) + b_1 \ln (V_0\theta_1/D_{c1}) + b_2 \ln (V_0\theta_2/D_{c2}) \quad (2)$$

$$d\theta_i/dt = 1 - (V\theta_i/D_{ci}), \ (i = 1, 2), \quad (3)$$

where $a$, $b_1$, and $b_2$ are the empirically derived constants (dimensionless); $\theta_1$ and $\theta_2$ are the state variables (units of time); and $D_{c1}$ and $D_{c2}$ are the critical slip distances. Most of our data are fit well with a one-state variable friction law ($D_{c2} = D_{c1}$, and thus, $b_2 = \theta_2 = 0$). However, some of our data required two state variables. We report values of $(a - b)$ and define $b = b_1 + b_2$ in the case of two state variables. We used the two-state variable friction law when the raw data could not be adequately fit with the one-state variable friction law. In most cases, this is evident from the existence of friction evolution over both short and long distances. Moreover, in these cases the friction inversions did not converge; in other cases, even if the solution converged within a specified overall error/misfit, the model produced a poor fit to the raw data on the basis of visual examination. Our goal in inverting for the rate and state parameters was to determine $a$, $b$, and $D_c$ from the experimental data. Uncertainty in the stiffness of the loading system has been shown to have nontrivial affects on the determined rate and state parameters [*Noda and Shimamoto*, 2009]. In order to reduce this error, in our inversions we begin with the measured stiffness of the apparatus based on the applied vertical load (that is, accounting for nonlinearity in stiffness at low loads) and then measure the stiffness for each velocity step and allow for minor changes that may arise from thinning of the layer and changes in porosity. Furthermore, while not the goal of this study, we note that there is a variety of "designer" friction laws that have been invoked to describe possible physical mechanisms underlying complex responses to velocity perturbations [e.g., *Reinen et al.*, 1991; *Kato and Tullis*, 2001; *Niemeijer and Spiers*, 2007].

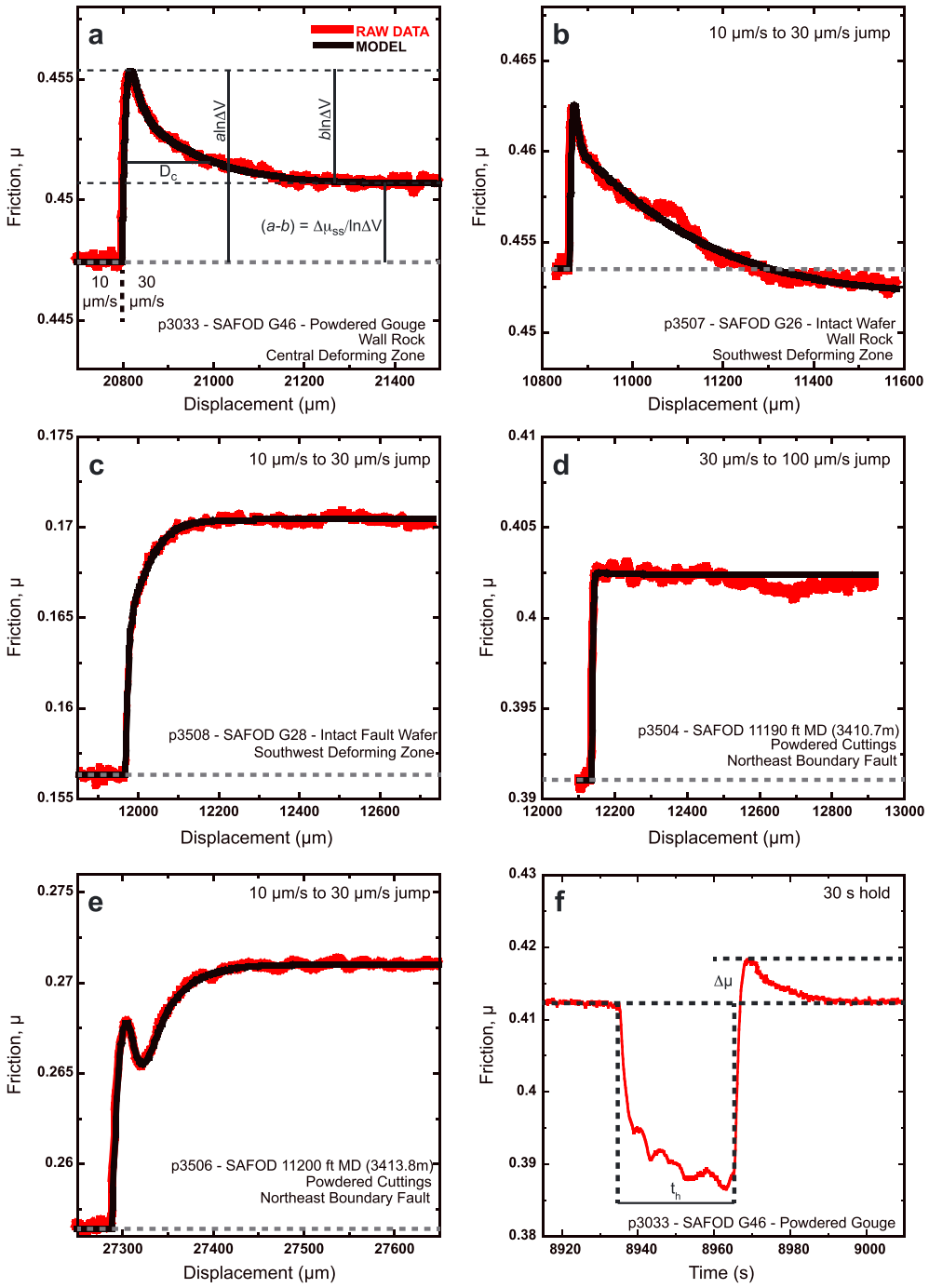


**Figure 5.** Raw data and modeling results for velocity step tests for (a) powdered gouge of wall rock near the CDZ, (b) an intact wafer of wall rock near the SDZ, (c) an intact wafer from the SDZ, and (d and e) powdered cuttings in the vicinity of the NBF. All data are for 25 MPa effective normal stress and for the velocities given. Details of RSF parameters are shown in Figure 5a. (f) Details of measured frictional healing parameters for an example slide-hold-slide test on material from near the CDZ; slide/reload velocity was 10 μm/s.

Examples of fits to five velocity steps (at 25 MPa effective normal stress) are shown in Figure 5. Figures 5a and 5b show velocity-strengthening and velocity-weakening friction behaviors, respectively, in which the friction parameters *a* and *b* are both positive. In both cases, a two-state variable friction law fits the data better and reflects two stages of evolution, one over a short critical slip distance (<20 μm) and another over a longer critical slip distance of >100 μm. We also observe behavior in which the parameter *b* is best fit by a

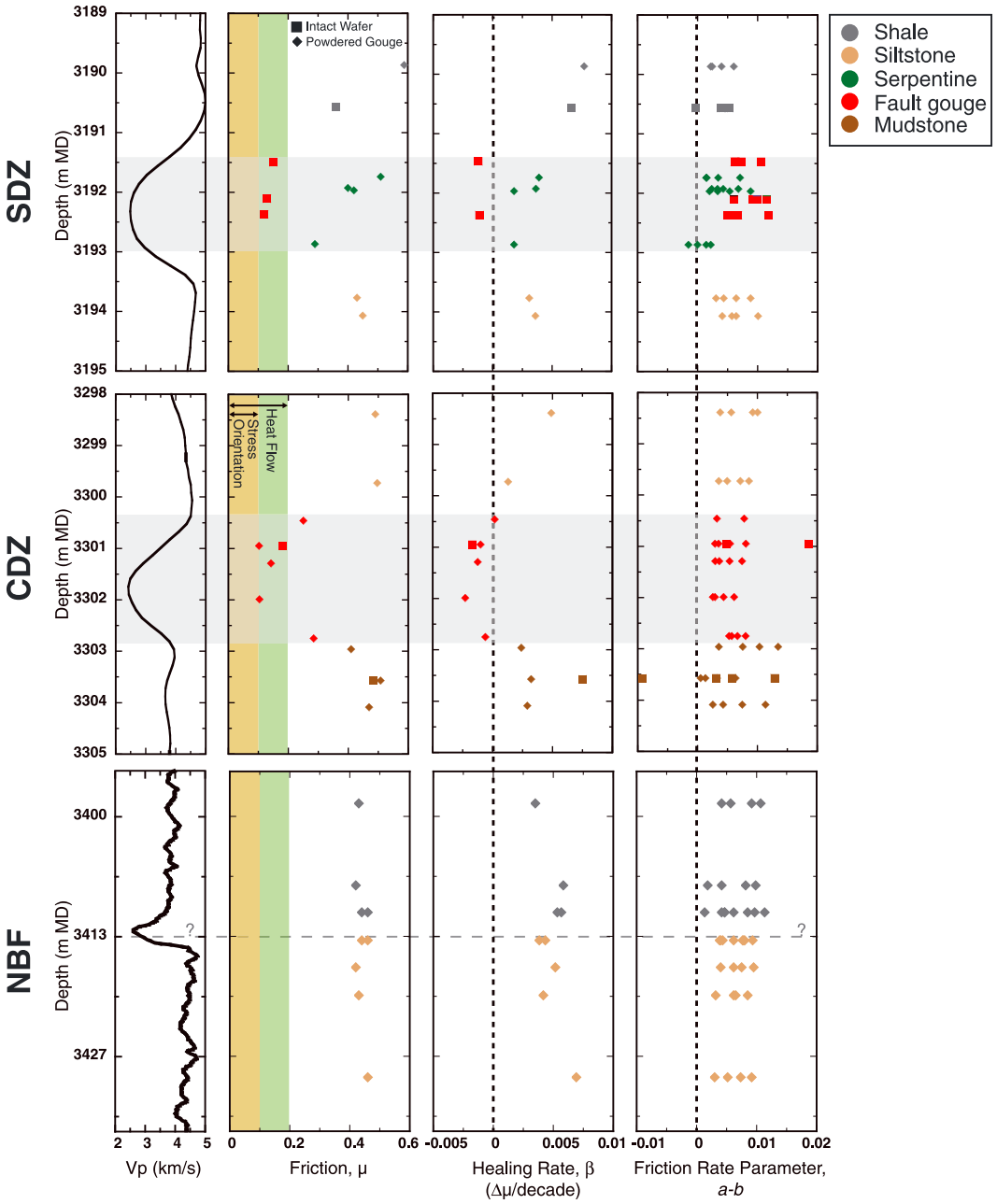


**Figure 6.** Summary of frictional strength, friction rate parameter ($a - b$), and frictional healing rate ($\beta$) for the three fault strands, with *P* wave velocity for reference. The symbols are colored based on lithology [*Solum et al*., 2006; *SAFOD*, 2010]. All data are for 25 MPa effective normal stress. The gray shaded areas indicate the locations of the SDZ and CDZ based on recovered core and geophysical logs; the dashed line shows the interpreted location of the NBF from geophysical logs. The green and yellow shaded areas indicate the limits on the effective friction coefficient interpreted from heat flow measurements [*Lachenbruch and Sass*, 1980] and directional constraints [*Zoback et al*., 1987].

negative value (Figure 5c) or is zero (Figure 5d). Finally, in some cases, two state variables are needed to explain the data, with $b_1$ and $b_2$ having opposite signs (Figure 5e) [*Noda and Shimamoto*, 2009]. In the velocity step shown in Figure 5e, we find $(a - b_1) = 0.0007$, indicating near-velocity neutral behavior, with $D_{c1} = 8\,\mu$m. However, the overall behavior shows $a - (b_1 + b_2) = 0.0121$, reflecting strong velocity-strengthening behavior over larger slip distances, with $D_{c2} = 23\,\mu$m.

Slide-hold-slide tests are used to determine the rate of frictional healing ($\beta$):

$$\beta = \Delta\mu / \log_{10} t_h, \quad (4)$$

where $\Delta\mu$ is the increase in peak friction after a hold of time $t_h$, relative to the initial value of sliding friction (Figure 5f). Both positive healing rates and velocity-weakening friction behavior are required for repeated earthquakes [*Brace and Byerlee*, 1966; *Dieterich*, 1978].

## 3. Results

Our results show that the SDZ and CDZ are both weak relative to the surrounding wall rock and weak in an absolute sense, with $\mu$ = ~0.1 (Figures 6 and 7, Table 1, and Table S2). Additionally, these two fault strands exhibit low to negative healing rates and velocity-strengthening frictional behavior (Figure 6), both of which are consistent with the observation of aseismic creep. Serpentine samples from within the SDZ and wall rock near both the SDZ and CDZ exhibit velocity-weakening friction for some experimental conditions, raising the possibility that they may be capable of hosting earthquake nucleation. In contrast, the NBF is frictionally stronger, with $\mu$ = 0.46, and we observe no clear changes in frictional strength or constitutive parameters across the fault. However, these measurements were only conducted on cuttings, so sample mixing and the loss of some clays are likely. Our results and their implications for fault behavior are discussed more fully below.

### 3.1. Southwest Deformation Zone

Intact fault rock from the SDZ exhibits friction coefficients ranging from $\mu$ = 0.12 to 0.15 (Figure 6). These friction values are slightly lower than those previously reported for powdered core from the SDZ ($\mu$ = 0.15–0.21) [*Lockner et al.*, 2011], suggesting that in situ fabric could be important in controlling fault strength and frictional properties [e.g., *Collettini et al.*, 2009; *Niemeijer et al.*, 2010]. Samples of powdered serpentine, obtained from large serpentine blocks within the fault gouge, exhibit steady state friction coefficients of $\mu$ = 0.29–0.51, and their friction decreases with increasing chrysotile content (Figures 4a and 6, Table 1, and Table S1).

Our data show that within 1 m of the actively creeping fault, frictional strength increases abruptly to values of $\mu > 0.35$, consistent with friction coefficients for shale and siltstone lithologies [e.g., *Ikari et al.*, 2009, 2011]. We find a near-zero or slightly negative healing rate for intact samples from the actively creeping fault, consistent with previous experiments on similar material recovered from the CDZ [*Carpenter et al.*, 2011, 2012]. The frictional healing rate is positive for the serpentine blocks from the fault zone, and for wall rock on both sides of the active fault ($0.0018 \leq \beta \leq 0.0077$), with the lowest rates observed in the chrysotile-rich serpentine (Figure 6). Intact wafers of SDZ gouge exhibit strong velocity-strengthening behavior ($a - b = 0.005$–$0.012$). The serpentine and wall rock samples also generally exhibit velocity-strengthening behavior ($0.002 \leq a - b \leq 0.010$), although a few instances of velocity-weakening friction behavior are observed for one serpentine sample from the fault and one wall rock sample from the SW ($-0.0015 \leq a - b \leq 0.005$).

### 3.2. Central Deformation Zone

Our experimental data set shows that the center of the CDZ is the weakest section of the San Andreas Fault, with $\mu$ = ~0.10 (Figure 6). Furthermore, fault weakness is highly localized to the CDZ, with an abrupt increase to higher strength ($\mu$ = 0.41–0.51) within the wall rock over distances of ~10 cm, consistent with previous work [*Lockner et al.*, 2011; *Carpenter et al.*, 2012; *Coble et al.*, 2014; *French et al.*, 2015]. Here we expand upon previous work [*Carpenter et al.*, 2012] with additional measurements that provide improved spatial resolution of frictional strength and constitutive properties across the fault and for a broader range of normal stresses and velocities (Figure 6). Additionally, we also report data for the individual friction rate parameters, $a$ and $b$.

Frictional healing is negative or zero within the CDZ fault ($-0.0022 \leq \beta \leq 0.0002$), but is positive in the immediately adjacent wall rock ($0.0024 \leq \beta \leq 0.0075$), with the largest healing rate in a sample to the NE. Material from the CDZ exhibits velocity-strengthening friction behavior ($0.026 \leq a - b \leq 0.018$), consistent with active fault creep observed near SAFOD and in the borehole. In many instances, material from the CDZ exhibits negative values of the friction evolution parameter $b$ ($-0.055 \leq b \leq 0.0015$; Figures 7 and 8 and Table S2). Wall rock samples

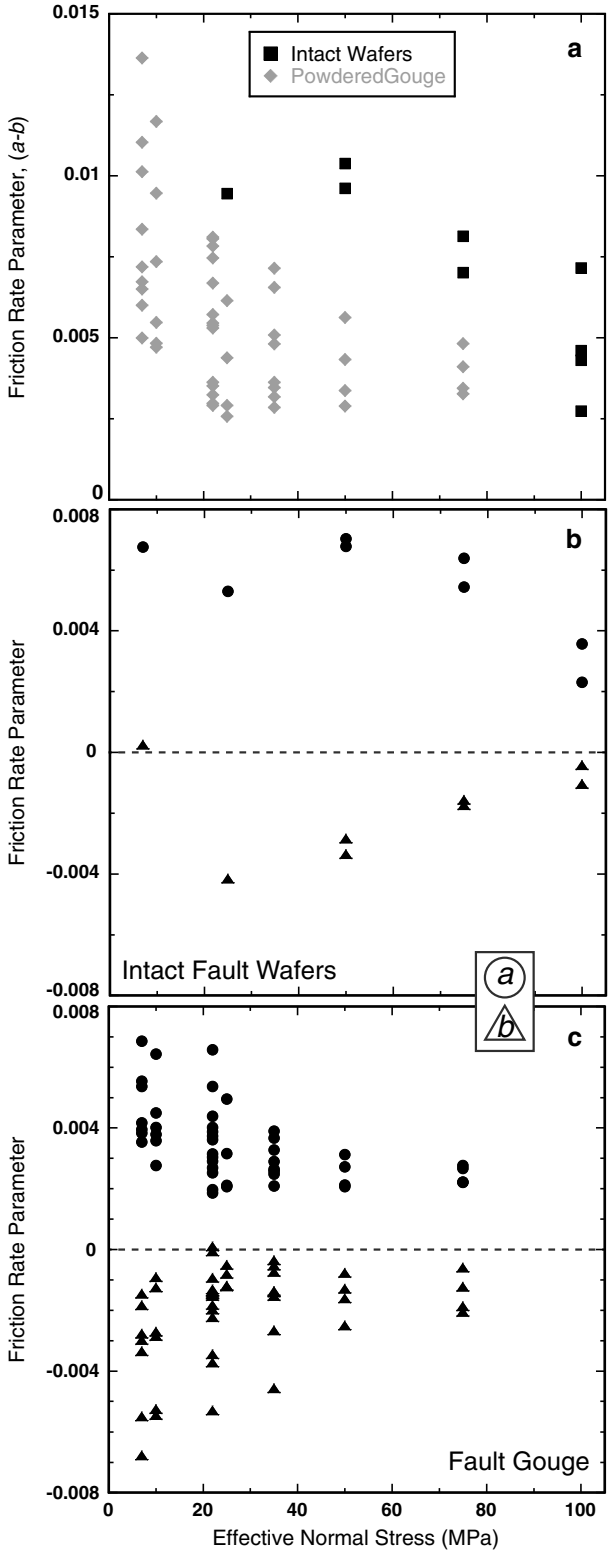


**Figure 7.** (a) Friction rate parameter ($a - b$) as a function of effective normal stress for material from the CDZ. Values of the individual rate parameters $a$ (circles) and $b$ (triangles) for (b) intact wafers and for (c) powdered gouge. Note that the state evolution parameter $b$ is negative for a wide range of conditions for both intact fault rock and for powdered fault rock and gouge. The steady state rate dependence of friction ($a - b$) is therefore positive, although it decreases with increasing normal stress.

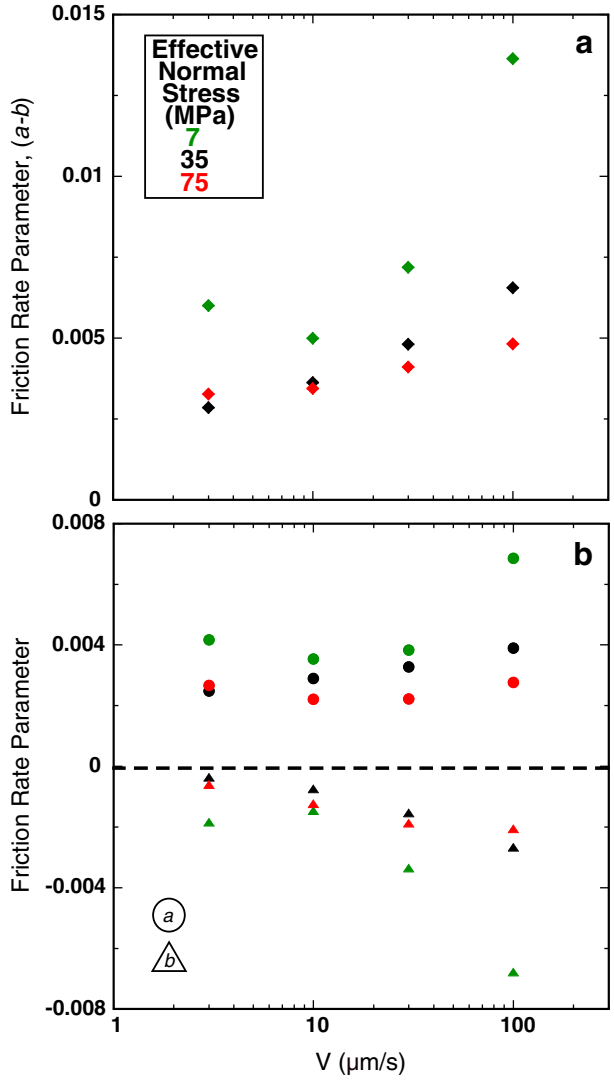


**Figure 8.** (a) Friction rate parameter, $(a-b)$, as a function of velocity ($V$) for powdered gouge from the CDZ at three different effective normal stresses. (b) Values of the individual rate parameters $a$ (circles) and $b$ (triangles).

show mainly velocity-strengthening behavior ($0.001 \leq a-b \leq 0.013$) with one case of velocity weakening, $(a-b) = -0.009$ in a sample from the NE side of the CDZ. We find that intact fault rock and powders of the same material exhibit similar values of friction coefficient, healing, and velocity dependence.

Taken together, our data and the results previously reported by *Carpenter et al.* [2012] show that for the CDZ, the friction rate parameter $(a-b)$ generally decreases with increasing normal stress (Figure 7a), although all samples remain in the velocity-strengthening regime. This is consistent with the results of experiments on similar clay-rich gouges that show values of $(a-b) = 0.002$ at elevated temperature and stress [*Lockner et al.*, 2011; *Coble et al.*, 2014]. For both intact and powdered samples, the parameter $b$ remains near zero or negative and systematically approaches zero with increasing effective normal stress (Figures 7b and 7c). The behavior of the parameter $a$ is more complex; for intact wafers of fault material, $a$ remains nearly constant to 70 MPa effective normal stress and decreases at higher stress (100 MPa), whereas for powdered gouge, it decreases with effective normal stress below ~50 MPa and remains approximately constant at higher normal stresses (Figure 7).

Our data show that within the range of velocities we explored (1–300 μm/s), both $a$ and $b$ approach zero as normal stress increases, with the greatest difference in their magnitudes occurring at the lowest effective normal stress (Figures 7b and 7c). Furthermore, for powdered gouge, $a$, $b$, and $(a-b)$ vary with sliding velocity, such that the friction rate parameter $(a-b)$ increases with increasing sliding velocity (Figures 8a and 8b). This effect is most pronounced at low effective normal stress and decreases with increasing stress. Our values are broadly consistent with other reported values of $a$, $b$, and $(a-b)$ in experiments performed on natural smectite-rich claystones at similar effective normal stresses [e.g., *Ikari and Saffer*, 2011].

### 3.3. Northeast Boundary Fault

Our data show that frictional strength is nearly uniform across the NBF, with friction coefficients ranging from $\mu = 0.42$ to 0.46 (Figure 6), consistent with previously reported values [*Tembe et al.*, 2006]. The rate of frictional healing is also nearly constant across the NBF, with values of $\beta$ in the range of 0.0040–0.0055. Overall, samples surrounding the NBF exhibit frictional healing rates of ($0.0035 \leq \beta \leq 0.0070$). We observe uniformly velocity-strengthening behavior ($0.001 \leq a-b \leq 0.011$) for these samples, with the minimum values for samples immediately to the SW of the fault, obtained at the slowest (1–3 μm/s) velocity steps (Figure 6).

## 4. Implications for Strength and Slip Behavior of the SAF

The overall mechanical behavior of the San Andreas Fault near Parkfield, CA, depends on the properties of all three active fault strands intersected in the SAFOD borehole. At the location of the borehole, the 1.5 m wide SDZ and 2.6 m wide CDZ are actively creeping [*Zoback et al*., 2011]. The CDZ is thought to be the main strand of the active SAF accommodating plate motion [*Zoback et al*., 2011; *Moore*, 2014]. Our experimental results are consistent with these observations: in that, (1) both the CDZ and SDZ are frictionally weak, (2) both exhibit friction constitutive behavior favoring aseismic (stable) sliding, and (3) the CDZ exhibits the lowest strength of the three strands. Our data also document velocity-weakening friction behavior in wall rock to the SW side of the CDZ, and we identify complex rate-dependent behavior in material near NBF, both of which may help explain the occurrence of repeating small earthquakes on the NBF [e.g., *Carpenter et al*., 2012].

The rate-dependent behavior we observe for material from within the CDZ, and its evolution with normal stress, suggests that ruptures initiating to the south, such as the 2004 Parkfield earthquake [*Langbein et al*., 2005], would likely propagate into the CDZ at depth where the frictional strength is low and the velocity dependence of friction is slightly positive. In this scenario, we expect that propagation to the surface would be inhibited because the gouge becomes increasingly velocity strengthening at low normal stress and at higher velocities. This is consistent with models of coeseismic and postseismic slip for the 2004 Parkfield earthquake that show propagation of seismic slip into the transition zone near SAFOD, followed by significant postseismic slip that increases with depth [*Johanson et al*., 2006].

The behavior of the fault at the SAFOD site is likely complicated due to its location between the locked section to the south and the creeping section of the SAF [*Zoback et al*., 2011, and references therein]. Although our mechanical data are consistent with the CDZ exhibiting the largest amount of casing deformation, creep on the SDZ and repeating earthquakes on both the SDZ and NBF indicate that these faults also accommodate strain. The interaction of these fault strands is likely to be complicated in this region, because fault slip transitions from dominantly seismogenic, south of Parkfield, to aseismic creep, north of SAFOD, and perhaps due to geometric complexity along strike. If the SDZ and CDZ are indeed coalescing strands of the SAF and extend farther to the north [*Moore and Rymer*, 2012], the creeping of these faults could be loading slivers of the Great Valley Sequence or serpentine that act as competent bodies at depth [*Fagereng and Sibson*, 2010; *Collettini et al*., 2011]. If that is the case, materials related to the locked section, or perhaps the serpentine hypothesized to be present along the entire creeping section [*Allen*, 1968; *Irwin and Barnes*, 1975], could form asperities at depth, leading to the observed mixed-mode behavior of fault failure. For example, modeling studies using rate and state friction parameters similar to those reported here show that the aseismic loading of velocity-weakening fault patches reproduces the repeating earthquakes observed near the SAFOD borehole [*Marone et al*., 1995; *Marone*, 1998b; *Chen and Lapusta*, 2009]. These asperities are one possible cause of the observed repeating earthquake clusters that have been mapped to the SDZ, approximately 100 m below the borehole, and on the NBF [*Thurber et al*., 2010].

Although extrapolation of our laboratory data to different portions of the SAF system or to greater depths is complicated by heterogeneity in composition and in situ conditions, our data, taken together with observations from drilling and previous work, provide a basis for linking experimental measurements to the behavior of the broader SAF system. In particular, the fact that fault gouge used for this study was collected from seismogenic depths, and that our work includes experiments on intact core sheared in its in situ geometry, facilitates comparisons between our data and the fault's in situ characteristics. Likewise, experiments performed at elevated temperature on similar samples produce nearly identical results to ours, further suggesting that our data are representative of the in situ fault zone and may be extrapolated to greater depths [*Lockner et al*., 2011; *Coble et al*., 2014; *French et al*., 2015]. One key result of our work is that the Mg-rich smectite (saponite) present in the SDZ and CDZ, formed by interaction of magnesium-rich fluids derived from serpentine with the quartzofeldspathic rocks of the Great Valley sequence [e.g., *Schleicher et al*., 2008; *Moore*, 2014], is frictionally weak and exhibits no healing. The identification of similar gouge along the SAF to the north [*Moore and Rymer*, 2012], and the observation that creeping segments of the SAF all throughout California coincide with locations where serpentine abuts the fault at depth [*Allen*, 1968; *Irwin and Barnes*, 1975], suggests that saponite could play an important role in the behavior of

the SAF system in other areas. Previous work has also suggested that saponite could be stable to temperatures >200°C, corresponding to depths of 5–8 km along the San Andreas [e.g., *Inoue and Utada*, 1991; *Schleicher et al*., 2012]. At greater depths, talc and brucite, which also exhibit low-friction coefficients, stable sliding behavior, and low frictional healing, could be present and cause fault weakness and aseismic creep where saponite is no longer stable [e.g., *Moore and Lockner*, 2004].

The low frictional strength of material from the actively creeping SDZ and CDZ is consistent with constraints on fault shear strength from measurements of heat flow and stress orientation [*Lachenbruch and Sass*, 1980; *Zoback et al*., 1987; *Scholz*, 2006] which show that along much of its length, the SAF supports depth-averaged shear stresses of <10–20 MPa, corresponding to an effective friction coefficient of <0.1–0.2. The observation of pressure-independent strength above normal stresses of ~40 MPa [*Carpenter et al*., 2012] and the likely occurrence of magnesium-rich smectite clays to depths of >5 km [*Schleicher et al*., 2012] further indicate that the behavior we document could explain low in situ shear strength to depths well into the seismigenic crust. These findings are also generally consistent with previous work that has suggested that the central creeping section of the SAF is weak, whereas other segments may be frictionally stronger [e.g., *Scholz*, 2000, 2006].

In terms of rate-dependent behavior, which is thought to control the mode of fault slip, behavior with no state evolution ($b = 0$) has been observed for clay-rich gouge at high normal stresses by *Saffer and Marone* [2003], who attributed it to saturation of the real area of contact. Negative values of $b$ have also been observed previously [*Blanpied et al*., 1998; *Ikari et al*., 2009; *Sone et al*., 2012], yet are not well explained by the widely held idea that real contact area decreases with increasing slip velocity and that the state evolution parameter $b$ tracks this change [e.g., *Saffer and Marone*, 2003]. Although the microphysical foundations of frictional state evolution are clearly important (for recent works, see *Nagata et al*. [2008], *Putelat et al*. [2011], *Bhattacharya and Rubin* [2014], and *Marone and Saffer* [2015]), they are beyond the scope of this paper. We note that several other "frictional-viscous" and coupled friction/flow laws have been proposed [*Reinen et al*., 1992; *Bos and Spiers*, 2002; *Noda and Shimamoto*, 2010; *Takahashi et al*., 2011], but these are focused primarily on special cases, and we do not consider them further here. Finally, *Horowitz* [1988], *Noda and Shimamoto* [2009], and *Ikari et al*. [2013] discussed mixed frictional behavior and suggested that some material may be potentially unstable over short slip distances but stable over longer slip distances. This may be the case in some of our samples and may warrant further study.

## 5. Summary

In total, our results document a complex set of frictional behaviors for the three faults penetrated in the SAFOD borehole and provide a consistent explanation for many of the observed fault behaviors, including absolute and relative fault weakness, highly localized active deformation, active creep along the SDZ and CDZ, and microearthquakes along the extension of the NBF. Material from both actively creeping strands (the SDZ and CDZ) is frictionally weak ($\mu = 0.1$), exhibits no frictional healing, and is velocity strengthening, all consistent with observations of low fault strength and creep. The weakness of these faults is highly localized, with frictional strength increasing to values $\mu > 0.4$ within <1 m into the wall rock. We also observe potentially unstable frictional behavior in wall rock near both the SDZ and CDZ and in serpentine located within the SDZ, suggesting that these materials might be involved in repeating earthquake clusters observed near the SAFOD borehole. Our work presents a comprehensive view of the behavior of the San Andreas Fault at the SAFOD site and expands on previous work by showing how fault properties will vary with depth in the shallow crust.

**Acknowledgments**
This research was funded by NSF awards EAR-054570, EAR-0746192, and OCE-0648331 to D.S. and C.M. We thank C. Scholz, N. Brantut, and one anonymous reviewer for their comments, which helped improve this manuscript. Data will be made available to interested parties via the corresponding author.

## References

Allen, C. R. (1968), The tectonic environments of seismically active and inactive areas along the San Andreas fault system, in *Proc. of Conf. on Geologic Problems of the San Andreas Fault System*, Univ. Ser., vol. 11, edited by. W. R. Dickinson and A. Grantz, pp. 70–82, Stanford Univ. Publ., Geol. Sci., Stanford, Calif.

Bhattacharya, P., and A. M. Rubin (2014), Frictional response to velocity steps and 1-D fault nucleation under a state evolution law with stressing-rate dependence, *J. Geophys. Res. Solid Earth*, *119*, 2272–2304, doi:10.1002/2013JB010671.

Blanpied, M. L., C. J. Marone, D. A. Lockner, J. D. Byerlee, and D. P. King (1998), Quantitative measure of the variation in fault rheology due to fluid rock interactions, *J. Geophys. Res.*, *103*, 9691–9712, doi:10.1029/98JB00162.

Bos, B., and C. J. Spiers (2002), Frictional-viscous flow of phyllosilicate-bearing fault rock: Microphysical model and implications for crustal strength profiles, *J. Geophys. Res.*, *107*(B2)s, B22028, doi:10.1029/2001JB000301.

Brace, W. F., and J. D. Byerlee (1966), Stick–slip as a mechanism for earthquakes, *Science*, *153*, 990–992.
Bradbury, K. K., J. P. Evans, J. S. Chester, F. M. Chester, and D. L. Kirschner (2011), Lithology and internal structure of the San Andreas Fault at depth based on characterization of Phase 3 whole-rock core in the San Andreas Fault Observatory at Depth (SAFOD) borehole, *Earth Planet. Sci. Lett.*, *310*, 131–144, doi:10.1016/j.epsl.2011.07.020.
Brantut, N., A. Schubnel, and Y. Guéguen (2011), Damage and rupture dynamics at the brittle-ductile transition: The case of gypsum, *J. Geophys. Res.*, *116*, B01404, doi:10.1029/2010JB007675.
Brown, K., A. Kopf, M. Underwood, and J. Weinberger (2003), Compositional and fluid pressure controls on the state of stress on the Nankai subduction thrust: A weak plate boundary, *Earth Planet. Sci. Lett.*, *214*, 589–603, doi:10.1016/S0012-821X(03)00388-1.
Brune, J. N., T. L. Henyey, and R. F. Roy (1969), Heat flow, stress, and rate of slip along the San Andreas Fault, California, *J. Geophys. Res.*, *74*, 3821–3827, doi:10.1029/JB074i015p03821.
Carpenter, B. M., C. Marone, and D. M. Saffer (2009), Frictional behavior of materials in the 3D SAFOD volume, *Geophys. Res. Lett.*, *36*, L05302, doi:10.1029/2008GL036660.
Carpenter, B. M., C. Marone, and D. M. Saffer (2011), Frictional strength of the San Andreas Fault from laboratory measurements of SAFOD drill samples, *Nat. Geosci.*, *4*, 251–254, doi:10.1038/ngeo1089.
Carpenter, B. M., D. M. Saffer, and C. Marone (2012), Frictional properties and sliding stability of the San Andreas Fault from deep drill core, *Geology*, *40*, 759–762, doi:10.1130/G33007.1.
Chen, T., and N. Lapusta (2009), Scaling of small repeating earthquakes explained by interaction of seismic and aseismic slip in a rate and state fault model, *J. Geophys. Res.*, *114*, B01311, doi:10.1029/2008JB005749.
Coble, C. G., M. E. French, F. M. Chester, J. S. Chester, and H. Kitajima (2014), In situ frictional properties of San Andreas Fault gouge at SAFOD, *Geophys. J. Int.*, *199*, 956–967, doi:10.1093/gji/ggu306.
Collettini, C., A. Niemeijer, C. Viti, and C. Marone (2009), Fault zone fabric and fault weakness, *Nature*, *462*, 907–910, doi:10.1038/nature08585.
Collettini, C., A. Niemeijer, C. Viti, S. A. F. Smith, and C. Marone (2011), Fault structure, frictional properties and mixed-mode fault slip behavior, *Earth Planet. Sci. Lett.*, *311*, 316–327, doi:10.1016/j.epsl.2011.09.020.
Dibblee, T. W. (1973), Regional geologic map of the San Andreas and related faults in Carrizo Plain, Temblor, Caliente, and La Panza ranges and vicinity, California, U.S. Geol. Surv. Miscellaneous Geologic Investigations, Map I-757.
Dieterich, J. H. (1978), Time-dependent friction and the mechanics of stick–slip, *Pure Appl. Geophys.*, *116*, 790–805.
Dieterich, J. H. (1979), Modeling of rock friction: 1. Experimental results and constitutive equations, *J. Geophys. Res.*, *84*, 2161–2168, doi:10.1029/JB084iB05p02161.
Fagereng, A., and R. H. Sibson (2010), Mélange rheology and seismic style, *Geology*, *38*, 751–754, doi:10.1130/G30868.1.
Faulkner, D. R., and E. H. Rutter (2001), Can the maintenance of overpressured fluids in large strike-slip fault zones explain their apparent weakness?, *Geology*, *29*, 503–506, doi:10.1130/0091-7613(2001)029<0503.CTMOOF>2.0.CO;2.
French, M. E., F. M. Chester, and J. S. Chester (2015), Micromechanisms of creep in clay-rich gouge from the Central Deforming Zone of the San Andreas Fault, *J. Geophys. Res. Solid Earth*, *120*, 827–849, doi:10.1002/2014JB011496.
Gratier, J.-P., J. Richard, F. Renard, S. Mittempergher, M.-L. Doan, G. Di Toro, J. Hadizadeh, and A.-M. Boullier (2011), Aseismic sliding of active faults by pressure solution creep: Evidence from the San Andreas Fault Observatory at Depth, *Geology*, *39*, 1131–1134, doi:10.1130/G32073.1.
Gu, J.-C., J. R. Rice, A. L. Ruina, and S. T. Tse (1984), Slip motion and stability of a single degree of freedom elastic system with rate and state dependent friction, *J. Mech. Phys. Solids*, *32*, 167–196.
Hadizadeh, J., S. Mittempergher, J.-P. Gratier, F. Renard, G. Di Toro, J. Richard, and H. A. Babaie (2012), A microstructural study of fault rocks from the SAFOD: Implications for the deformation mechanisms and strength of the creeping segment of the San Andreas Fault, *J. Struct. Geol.*, *42*, 246–260, doi:10.1016/j.jsg.2012.04.011.
Haines, S. H., B. Kaproth, C. Marone, D. Saffer, and B. A. van der Pluijm (2013), Shear zones in clay-rich fault gouge: A laboratory study of fabric development and evolution, *J. Struct. Geol.*, *51*, 206–225, doi:10.1016/j.jsg.2013.01.002.
Hickman, S., and M. Zoback (2004), Stress orientations and magnitudes in the SAFOD pilot hole, *Geophys. Res. Lett.*, *31*, L15S12, doi:10.1029/2004GL020043.
Hickman, S., M. D. Zoback, and W. Ellsworth (2004), Introduction to special issue: Preparing for the San Andreas Fault Observatory at Depth, *Geophys. Res. Lett.*, *31* L12S01, doi:10.1029/2004GL020688.
Holdsworth, R. E., E. W. E. van Diggelen, C. J. Spiers, J. H. P. de Bresser, R. J. Walker, and L. Bowen (2011), Fault rocks from the SAFOD core samples: Implications for weakening at shallow depths along the San Andreas Fault, California, *J. Struct. Geol.*, *33*, 132–144, doi:10.1016/j.jsg.2010.11.010.
Horowitz, F. G. (1988), Mixed state variable friction laws: Some implications for experiments and stability analysis, *Geophys. Res. Lett.*, *15*, 1243–1246, doi:10.1029/GL015i011p01243.
Ikari, M. J., and D. M. Saffer (2011), Comparison of frictional strength and velocity dependence between fault zones in the Nankai accretionary complex, *Geochem. Geophys. Geosyst.*, *12*, Q0AD11, doi:10.1029/2010GC003442.
Ikari, M. J., D. M. Saffer, and C. Marone (2009), Frictional and hydrologic properties of clay-rich fault gouge, *J. Geophys. Res.*, *114*, B05409, doi:10.1029/2008JB006089.
Ikari, M. J., C. Marone, and D. M. Saffer (2011), On the relation between fault strength and frictional stability, *Geology*, *39*, 83–86, doi:10.1130/G31416.1.
Ikari, M. J., C. Marone, D. Saffer, and A. Kopf (2013), Slip weakening as a mechanism for slow earthquakes, *Nat. Geosci.*, *6*, 468–472, doi:10.1038/ngeo1818.
Inoue, A., and M. Utada (1991), Smectite-to-chlorite transformation in thermally metamorphosed volcaniclastic rocks in the Kamikita area, northern Honshu, Japan, *Am. Mineral.*, *79*, 628–640.
Irwin, W. P., and I. Barnes (1975), Effect of geologic structure and metamorphic fluids on seismic behavior of the San Andreas fault system in central and northern California, *Geology*, *3*, 713–716.
Johanson, I. A., E. J. Fielding, F. Rolandone, and R. Bürgmann (2006), Coseismic and postseismic slip of the 2004 Parkfield earthquake from space geodetic data, *Bull. Seismol. Soc. Am.*, *96*, 269–282, doi:10.1785/0120050818.
Kato, N., and T. E. Tullis (2001), A composite rate- and state-dependent law for rock friction, *Geophys. Res. Lett.*, *28*, 1103–1106, doi:10.1029/2000GL012060.
Kinoshita, M., H. Tobin, J. Ashi, G. Kimura, S. Lallemant, E. J. Screaton, D. Curewitz, H. Masago, K. T. Moe, and the Expedition 314/315/316 Scientists (2009), *IODP Proceedings, 314/315/316*, Integrated Ocean Drilling Program Management International, Inc., Washington, D. C., doi:10.2204/iodp.proc.314315316.134.2009.
Lachenbruch, A. H., and J. H. Sass (1980), Heat flow and energetics of the San Andreas fault zone, *J. Geophys. Res.*, *85*, 6185–6222, doi:10.1029/JB085iB11p06185.

Langbein, L., R. Borcherdt, D. S. Dreger, J. Fletcher, J. L. Hardebeck, J. R. Murray, R. Nadeau, M. J. Rymer, and J. A. Treiman (2005), Preliminary report on the 28 September 2004, *M* 6.0 Parkfield, California earthquake, *Seismol. Res. Lett.*, *76*, doi:10.1785/gssrl.76.1.10.

Lockner, D. A., C. Morrow, D. Moore, and S. Hickman (2011), Low strength of deep San Andreas Fault gouge from SAFOD core, *Nature*, *472*, 82–85, doi:10.1038/nature09927.

Logan, J., and K. Rauenzahn (1987), Frictional dependence of gouge mixtures of quartz and montmorillonite on velocity, composition, and fabric, *Tectonophysics*, *144*, 87–108, doi:10.1016/0040-1951(87)90010-2.

Lupini, J., A. Skinner, and P. Vaughan (1981), The drained residual strength of cohesive soils, *Geotechnique*, *31*, 181–213.

Marone, C. (1998a), Laboratory-derived friction laws and their application to seismic faulting, *Annu. Rev. Earth Planet. Sci.*, *26*, 643–696, doi:10.1146/annurev.earth.26.1.643.

Marone, C. (1998b), The effect of loading rate on static friction and the rate of fault healing during the earthquake cycle, *Nature*, *391*, 69–72, doi:10.1038/34157.

Marone, C., and D. Saffer (2015), The mechanics of frictional healing and slip instability during the seismic cycle, *Treatise Geophys.*, *4*, 111–138, doi:10.1016/B978-0-444-53802-4.00092-0.

Marone, C., J. E. Vidale, and W. L. Ellsworth (1995), Fault healing inferred from time dependent variations in source properties of repeating earthquakes, *Geophys. Res. Lett.*, *22*, 3095–3098, doi:10.1029/95GL03076.

Moore, D. E. (2014), Comparative mineral chemistry and textures of SAFOD fault gouge and damage-zone rocks, *J. Struct. Geol.*, *68*, 82–96, doi:10.1016/j.jsg.2014.09.002.

Moore, D. E., and D. A. Lockner (2004), Crystallographic controls on the frictional behavior of dry and water-saturated sheet structure minerals, *J. Geophys. Res.*, *109*, B03401, doi:10.1029/2003JB002582.

Moore, D. E., and M. J. Rymer (2012), Correlation of clayey gouge in a surface exposure of serpentinite in the San Andreas Fault with gouge from the San Andreas Fault Observatory at Depth (SAFOD), *J. Struct. Geol.*, *38*, 51–60, doi:10.1016/j.jsg.2011.11.014.

Morrow, C., J. Solum, S. Tembe, D. Lockner, and T. Wong (2007), Using drill cutting separates to estimate the strength of narrow shear zones at SAFOD, *Geophys. Res. Lett.*, *34*, L11301, doi:10.1029/2007GL029665.

Nagata, K., M. Nakatani, and S. Yoshida (2008), Monitoring frictional strength with acoustic wave transmission, *Geophys. Res. Lett.*, *35*, L06310, doi:10.1029/2007GL033146.

Niemeijer, A. R., and C. J. Spiers (2007), A microphysical model for strong velocity weakening in phyllosilicate-bearing fault gouges, *J. Geophys. Res.*, *112*, B10405, doi:10.1029/2007JB005008.

Niemeijer, A., C. Marone, and D. Elsworth (2010), Fabric induced weakness of tectonic faults, *Geophys. Res. Lett.*, *37*, L03304, doi:10.1029/2009GL041689.

Noda, H., and T. Shimamoto (2009), Constitutive properties of clayey fault gouge from the Hanaore fault zone, southwest Japan, *J. Geophys. Res.*, *114*, B04409, doi:10.1029/2008JB005683.

Noda, H., and T. Shimamoto (2010), A rate- and state-dependent ductile flow law of polycrystalline halite under large shear strain and implications for transition to brittle deformation, *Geophys. Res. Lett.*, *37*, L09310, doi:10.1029/2010GL042512.

Putelat, T., J. H. P. Dawes, and J. R. Willis (2011), On the microphysical foundations of rate-and-state friction, *J. Mech. Phys. Solids*, *59*, 1062–1075, doi:10.1016/j.jmps.2011.02.002.

Reinen, L. A., and J. D. Weeks (1993), Determination of rock friction constitutive parameters using an iterative least-squares inversion method, *J. Geophys. Res.*, *98*, 15,937–15,950, doi:10.1029/93JB00780.

Reinen, L. A., J. D. Weeks, and T. E. Tullis (1991), The frictional behavior of serpentinite: Implications for aseismic creep on shallow crustal faults, *Geophys. Res. Lett.*, *18*, 1921–1924, doi:10.1029/91GL02367.

Reinen, L. A., T. E. Tullis, and J. D. Weeks (1992), Two-mechanism model for frictional sliding of serpentine, *Geophys. Res. Lett.*, *19*, 1535–1538, doi:10.1029/92GL01388.

Rice, J. R. (1992), Fault stress states, pore pressure distributions, and the weakness of the San Andreas Fault, in *Fault Mechanics and Transport Properties of Rocks*, edited by B. Evan and T.-F. Wong, pp. 475–503, Academic Press, Ltd., San Diego, Calif.

Richard, J., J.-P. Gratier, M.-L. Doan, A.-M. Boullier, and F. Renard (2014), Rock and mineral transformations in a fault zone leading to permanent creep: Interactions between brittle and viscous mechanisms in the San Andreas Fault, *J. Geophys. Res. Solid Earth*, *119*, 8132–8153, doi:10.1002/2014JB011489.

Ruina, A. (1983), Slip instability and state variable friction laws, *J. Geophys. Res.*, *88*(B12), 10,359–10,370, doi:10.1029/JB088iB12p10359.

Saffer, D. M., and C. Marone (2003), Comparison of smectite- and illite-rich gouge frictional properties: Application to the updip limit of the seismogenic zone along subduction megathrusts, *Earth Planet. Sci. Lett.*, *215*, 219–235, doi:10.1016/S0012-821X(03)00424-2.

SAFOD (2010), Photographic atlas of the SAFOD 3 cores. [Available at http://earthscope.org/es_doc/data/safod/Core%20Photo%20Atlas%20v4.pdf]. version 4.

Schleicher, A. M., L. N. Warr, and B. A. van der Pluijm (2008), On the origin of mixed-layered clay minerals from the San Andreas Fault at 2.5–3 km vertical depth (SAFOD drillhole at Parkfield, California), *Contrib. Mineral. Petrol.*, *157*, 173–187, doi:10.1007/s00410-008-0328-7.

Schleicher, A. M., B. A. van der Pluijm, and L. N. Warr (2010), Nanocoatings of clay and creep of the San Andreas Fault at Parkfield, California, *Geology*, *38*, 667–670.

Schleicher, A. M., B. A. van der Pluijm, and L. N. Warr (2012), Chlorite-smectite clay minerals and fault behavior: New evidence from the San Andreas Fault Observatory at Depth (SAFOD) core, *Lithosphere*, *4*, 209–220, doi:10.1130/L158.1.

Scholz, C. H. (2000), Evidence for a strong San Andreas Fault, *Geology*, *28*, 163–166.

Scholz, C. H. (2006), The strength of the San Andreas Fault: A critical analysis, paper presented at Earthquakes: Radiated Energy and the Physics of Faulting, AGU Monograph 170.

Solum, J. G., S. H. Hickman, D. A. Lockner, D. E. Moore, B. A. van der Pluijm, A. M. Schleicher, and J. P. Evans (2006), Mineralogical characterization of protolith and fault rocks from the SAFOD Main Hole, *Geophys. Res. Lett.*, *33*, L21314, doi:10.1029/2006GL027285.

Sone, H., T. Shimamoto, and D. E. Moore (2012), Frictional properties of saponite-rich fault gouge from a serpentine-bearing fault zone along the Gokasho-Arashima Tectonic Line, central Japan, *J. Struct. Geol.*, *38*, 172–182, doi:10.1016/j.jsg.2011.09.007.

Takahashi, M., S.-I. Uehara, K. Mizoguchi, I. Shimizu, K. Okazaki, and K. Masuda (2011), On the transient response of serpentine (antigorite) gouge to step-wise changes in slip velocity under high-temperature conditions, *J. Geophys. Res.*, *116*, B10405, doi:10.1029/2010JB008062.

Tembe, S., D. Lockner, J. G. Solum, C. A. Morrow, T. Wong, and D. E. Moore (2006), Frictional strength of cuttings and core from SAFOD drill phases 1 and 2, *Geophys. Res. Lett.*, *33*, L23307, doi:10.1029/2006GL027626.

Thayer, M. R., J. R. Arrowsmith, J. J. Young, A. K. Fayon, and M. J. Rymer (2004), Geologic structure of Middle Mountain within the San Andreas Fault zone near Parkfield, California, *EOS Trans. AGU, 85*, 1335.

Thordsen, J. J., W. C. Evans, Y. K. Kharaka, B. M. Kennedy, and M. van Soest (2005), Chemical and isotopic composition of water and gases from the SAFOD wells: Implications to the dynamics of the San Andreas Fault at Parkfield, California, *Eos Trans. AGU, 86*, T23E-08.

Thurber, C. H., S. W. Roecker, H. Zhang, N. L. Bennington, and D. Peterson (2010), Crustal structure and seismicity around SAFOD: A ten-year perspective, *Eos Trans. AGU, 91*, T52B-01.

Titus, S. J., C. DeMets, and B. Tikoff (2006), Thirty-five-year creep rates for the creeping segment of the San Andreas Fault and the effects of the 2004 *M* 6.0 Parkfield earthquake: Constraints from alignment arrays, continuous GPS, and creepmeters, *Bull. Seismol. Soc. Am.*, *96*, 5250–5268, doi:10.1785/0120050811.

Townend, J., R. Sutherland, and V. G. Toy (2009), Deep Fault Drilling Project—Alpine Fault, New Zealand, *Sci. Drill.*, *8*, 75–82, doi:10.2204/iodp.sd.8.12.2009.

Warr, L. N., J. Wajatschke, B. M. Carpenter, C. Marone, A. Schleicher, and B. van der Pluijm (2014), A "slice-and-view" (FIB-SEM) study of clay gouge from the SAFOD creeping section of the San Andreas Fault at ~2.7 km depth, *J. Struc. Geol.*, *69*, 234–244, doi:10.1016/j.jsg.2014.10.006.

Zoback, M. D., et al. (1987), New evidence on the state of stress of the San Andreas Fault system, *Science*, *238*(4830), 1105–1111.

Zoback, M. D., S. Hickman, W. Ellsworth, and the SAFOD Science Team (2011), Scientific drilling into the San Andreas Fault Zone—An overview of SAFOD's first five years, *Sci. Drill.*, *11*, 14–28.